Journal of Alloys and Compounds 900 (2022) 163518

Contents lists available at ScienceDirect

Journal of Alloys and Compounds

journal homepage: www.elsevier.com/locate/jalcom

Low-crystallinity tungsten disulfide construction by in-situ confinement effect enables ultrastable sodium-ion storage

Lulu Mo[a], Mingyu Gao[a], Gangyong Zhou[a], Wei Zong[a], Ai-Long Chen[a], Xiaoshan Fan[a,*], Yue-E Miao[a,*], Tianxi Liu[a,b,*]

[a] State Key Laboratory for Modification of Chemical Fibers and Polymer Materials, College of Materials Science and Engineering, Donghua University, Shanghai 201620, China
[b] Key Laboratory of Synthetic and Biological Colloids, Ministry of Education, School of Chemical and Material Engineering, Jiangnan University, Wuxi 214122, China

ARTICLE INFO

Article history:
Received 15 September 2021
Received in revised form 27 December 2021
Accepted 27 December 2021
Available online 30 December 2021

Keywords:
Carbon nanofibers
Low-crystallinity WS_2
Electrospinning
Sodium-ion batteries
Cycling stability

ABSTRACT

As a typical metal sulfide, tungsten disulfide (WS_2) with high theoretical capacity has attracted significant attention as the anode for sodium-ion batteries (SIBs). However, WS_2 bulk material usually displays poor rate performance and fast capacity fading in practical applications due to its low conductivity and structural instability. Herein, we propose an in-situ confinement strategy for synthesizing low-crystallinity and ultrafine WS_2 nanosheets within carbon nanofibers (WS_2-CNF) by the simple heat treatment of electrospun polyacrylonitrile/ammonium tetrathiotungstate (PAN/$(NH_4)_2WS_4$) nanofibers. The low-crystallinity structure of WS_2 with ultrasmall size and rich defects can greatly reduce the volume change and shorten the ion diffusion length. WS_2 nanosheets are confined in the CNF matrix, which is capable of effectively improving its electronic conductivity and structural stability. Based on these advantages, the WS_2-CNF composite electrode demonstrates fast and ultrastable Na^+ storage performance with a high capacity of 182 mAh g^{-1} after 6000 cycles at 5.0 A g^{-1}. Therefore, this work provides a simple and facile strategy for developing high-performance WS_2 anodes for SIBs.

© 2021 Elsevier B.V. All rights reserved.

1. Introduction

Due to their advantages of low cost and similar electrochemical mechanism to lithium-ion batteries (LIBs), sodium-ion batteries (SIBs) are currently regarded as possible alternatives to LIBs, especially in the application of large-scale energy storage [1–4]. Nevertheless, because Na^+ has a larger radius (0.102 nm) than Li^+ (0.076 nm), the graphite anode of commercial LIBs is not directly used in SIBs [5,6]. Therefore, many new anode materials have been explored for the development of SIBs [7–10].

Currently, metal sulfides have shown great promising as the anode candidates for SIBs, which exhibit the higher theoretical capacity than carbon materials and better electrochemical reversibility than metal oxides [11–14]. Among them, two-dimensional layered WS_2 possesses the relatively wide interlayer spacing of 0.62 nm, weak interlayer forces and easily broken W-S bonds, which enables easier Na^+ insertion and phase-conversion reactions for Na^+ storage [15,16]. Theoretically, WS_2 should be suitable for use in SIBs. However, the practical application of WS_2 still exists some problems. Bulk WS_2 shows sluggish kinetics on account of long ion diffusion distance and inferior conductivity. This largely affects its rapid charging and discharging capability, thereby resulting in unsatisfactory rate performance [17]. Moreover, WS_2 with high crystallinity and large grain size often generates large volume variations during the cycling process, which causes irreversible damage to electrode materials and severe capacity fading [18].

To address the above-mentioned issues, the most commonly used strategy is the rational construction of nanostructures based on various carbon templates, which can not only inhibit the agglomeration of the active materials and but also improve conductivity [19–21]. For example, a cubic-shaped WS_2 composite was prepared by growing WS_2 nanosheets on the template of a porous carbon framework, which exhibited a high-rate capability [21]. It can be benefit from the enhanced electron conductivity and the decreased size of WS_2, giving a fast charge transfer. Zhang et al. synthesized a MoS_2/Mxene composite anchored on the carbonized kapok fiber (CKF) [22]. The MoS_2/Mxene heterostructure could provide rich Na^+

* Corresponding authors.
* Corresponding author at: State Key Laboratory for Modification of Chemical Fibers and Polymer Materials, College of Materials Science and Engineering, Donghua University, Shanghai 201620, China.
E-mail addresses: xsfan@dhu.edu.cn (X. Fan), yuee_miao@dhu.edu.cn (Y.-E. Miao), txliu@dhu.edu.cn (T. Liu).

https://doi.org/10.1016/j.jallcom.2021.163518
0925-8388/© 2021 Elsevier B.V. All rights reserved.

intercalation sites. Meanwhile, the CKF template acted as the support and relieved the volume effect caused by the phase change to effectively slow down the collapse of active materials. Therefore, the MoS_2/Mxene/CKF composite delivered higher Na^+ storage capacity and rate performance than that of pure MoS_2. However, through the surface-growth way, the active materials were partially combined with the substrate, which had a limited effect on mitigating the volume change. Thus, long cycling stability could not be guaranteed. In this respect, Wu et al. reported the heterogeneous FeS_2/WS_2 hybrid confined in the hollow carbon nanobox composite fibers (NB FeS_2/WS_2-CNFs) [23]. Owning to the space and interfacial confinement effects, the NB FeS_2/WS_2-CNFs achieved enhanced structure stability and a long cycling Na^+ storage capability of 422.6 mAh g^{-1} at 0.5 A g^{-1} after 500 cycles. Mao et al. designed a yolk-heteroshell structure composite by confining Sn nanoparticles in N-doped C nanocage and growing ultra-thin MoS_2 nanosheets on its surface [24]. It exhibited a highly reversible capacity of 350.6 mAh g^{-1} at 0.5 A g^{-1} after 500 cycles, which can be attributed to that the N-doped carbon skeleton could effectively release the mechanical stress/strain of Sn and MoS_2 during the repeated charge/discharge cycles.

Reducing the crystallinity of electrode materials is another effective strategy for tuning the intrinsic structure and improving the electrochemical performance. For instance, low-crystallinity VS_4 microspheres and amorphous Nb_2O_5 have been demonstrated to outperform their highly crystalline counterparts for Na^+ storage [25,26]. In detail, low-crystallinity or amorphous electrode materials with highly disordered structures and rich defects are helpful for intrinsically increasing the ion diffusion rate and relieving expansion stress. Based on previous researches, metal sulfides confined in the carbonous templates and the reduced intrinsic crystallinity are two efficient approaches to improve the Na^+ storage performance with fast ions/electrons diffusion rate and stable structure. However, it still remains a great challenge to synergistically regulate between the intrinsic crystallinity and physical confinement in constructing the advanced WS_2-based materials for SIBs.

Herein, a rational confinement strategy is adopted to synthesize low-crystallinity and ultrathin WS_2 nanosheet-embedded carbon nanofiber (WS_2-CNF) composites *via* the combination of a simple electrospinning technique with subsequent heat treatment. The nanofiber framework precursor can efficiently restrict from the stack growth of WS_2 to form the disordered and small-sized structure, thus achieving abundant active sites, short mass transfer pathways and small volume strain in SIBs. In addition, WS_2 nanosheets are uniformly and firmly confined to the CNF matrix, which can further suppress the agglomeration of WS_2 during cycles and reinforce its structural stability, thereby improving the cycling reversibility of WS_2 anode materials. Meanwhile, the excellent electron conductivity of carbon nanofibers also ensures rapid electron transfer for electrochemical reactions. Therefore, the well-designed WS_2-CNF anode achieves a high reversible capacity of 302 mAh g^{-1} over 100 cycles at 0.1 A g^{-1}, an excellent high-rate capacity of 194 mAh g^{-1} at 5.0 A g^{-1}, and a long-term cycling stability of 182 mAh g^{-1} after 6000 cycles. All the results indicate the feasibility of a confinement strategy for enhancing the rate and cycling performances of WS_2 anode materials for SIBs.

2. Experimental section

2.1. Material synthesis

WS_2-CNF composites were synthesized by electrospinning with subsequent heat treatment. In detail, 1.0 g of ammonium tetrathiotungstate ($(NH_4)_2WS_4$), 1.0 g of polyacrylonitrile (PAN, M_w = 150,000) and 10 mL of *N,N*-dimethylformamide (DMF) solvent were mixed in a bottle. After stirring at 25 °C for approximately 10 h, a homogeneous solution was obtained for electrospinning. The applied voltage was 15 kV, the feeding rate was 0.05 mm min^{-1}, and the spinneret-collector distance was set as 20 cm. The as-collected nanofiber membrane was first stabilized at 400 °C for 2 h at 2 °C min^{-1} in a reducing atmosphere (Ar/H_2, 95%/5%, v/v) and continually carbonized at 650 °C for 2 h at 5 °C min^{-1}. Finally, the WS_2-CNF composite was obtained. For comparison, pure WS_2 with high crystallinity and large grain size, signed as WS_2-bulk, was also obtained by directly annealing the as-purchased $(NH_4)_2WS_4$ precursor without an electrospinning process. The CNF membrane was also prepared by only using the polymer precursor.

2.2. Material characterizations

Morphologies of as-synthesized samples were observed by scanning electron microscope (SEM, JSM-7500F). The detailed internal structure of the samples was characterized by transmission electron microscope (TEM, FEI Talos F200S) equipped with an energy dispersive spectrometer (EDS). The N_2 adsorption/desorption measurements were carried out on an Autosorb-iQ instrument. The surface area was evaluated by Brunauer-Emmett-Teller (BET) theory, and the pore size was analyzed by Barrett–Joyner–Halenda (BJH) method. The crystalline structure and composition of the samples were analyzed by X-ray diffraction (XRD, D/Max2550VB), Raman (Renishaw inVia-Reflex spectrometer) and X-ray photoelectron spectroscopy (XPS, ESCALAB 250Xi). The WS_2 content in the composite was estimated by thermogravimetric analysis (TGA, 209 F1 Libra) under air atmosphere with 10 °C min^{-1}.

2.3. Electrochemical measurements

CR2025 half-cells were assembled to test electrochemical performances of the samples. For the preparation of working electrode, as-prepared sample, Super P and polyvinylidene fluoride with the mass ratio of 8:1:1 were mixed in the 1-methyl-2-pyrrolidinone solvent, and then casted onto copper foil with subsequent vacuum drying at 80 °C for 12 h. Unless otherwise noted, the mass loading of the active materials on each electrode was about 0.8 mg cm^{-2}. Sodium foil was employed as the counter electrode. Glass fiber (GF/D, Waterman) was used as the separator. Meanwhile, the electrolyte (DoDoChem.) was 1 M $NaClO_4$ dissolved in ethylene carbonate/dimethyl carbonate (1:1, v/v) with 5 wt% of fluoroethylene carbonate additive. Galvanostatic charge/discharge (GCD) measurements for the assembled cells were performed using the LAND-CT2001A battery-test system. Electrochemical impedance spectroscopy (EIS) and cyclic voltammetry (CV) tests were carried out on the CHI660E electrochemical workstation. The voltage range of all the electrochemical measurements was controlled in 0.01–3.0 V.

3. Results and discussion

3.1. Morphology and structure of the WS_2-CNF composites

The WS_2-CNF composites were obtained by heat treatment of electrospun $(NH_4)_2WS_4$-PAN precursor nanofibers in a reducing atmosphere of Ar/H_2, as illustrated in Fig. 1a. During the heat treatment, $(NH_4)_2WS_4$ and PAN were converted to WS_2 and carbon nanofibers, respectively. As the evolution of the $(NH_4)_2WS_4$ phase was well confined by the PAN phase, ultrafine WS_2 nanosheets were in-situ formed and uniformly embedded into the CNF matrix. As shown in Fig. S1, the as-spun $(NH_4)_2WS_4$-PAN composite nanofibers exhibit a uniform and interwoven fibrous network with a fiber diameter of about 170 nm. After high-temperature calcination, the obtained WS_2-CNF composite shows a slight shrinkage with a diameter around 140 nm but still maintains a good fiber shape (Fig. 1b, c). Compared with the pure CNF (Fig. S2), disordered and ultrafine

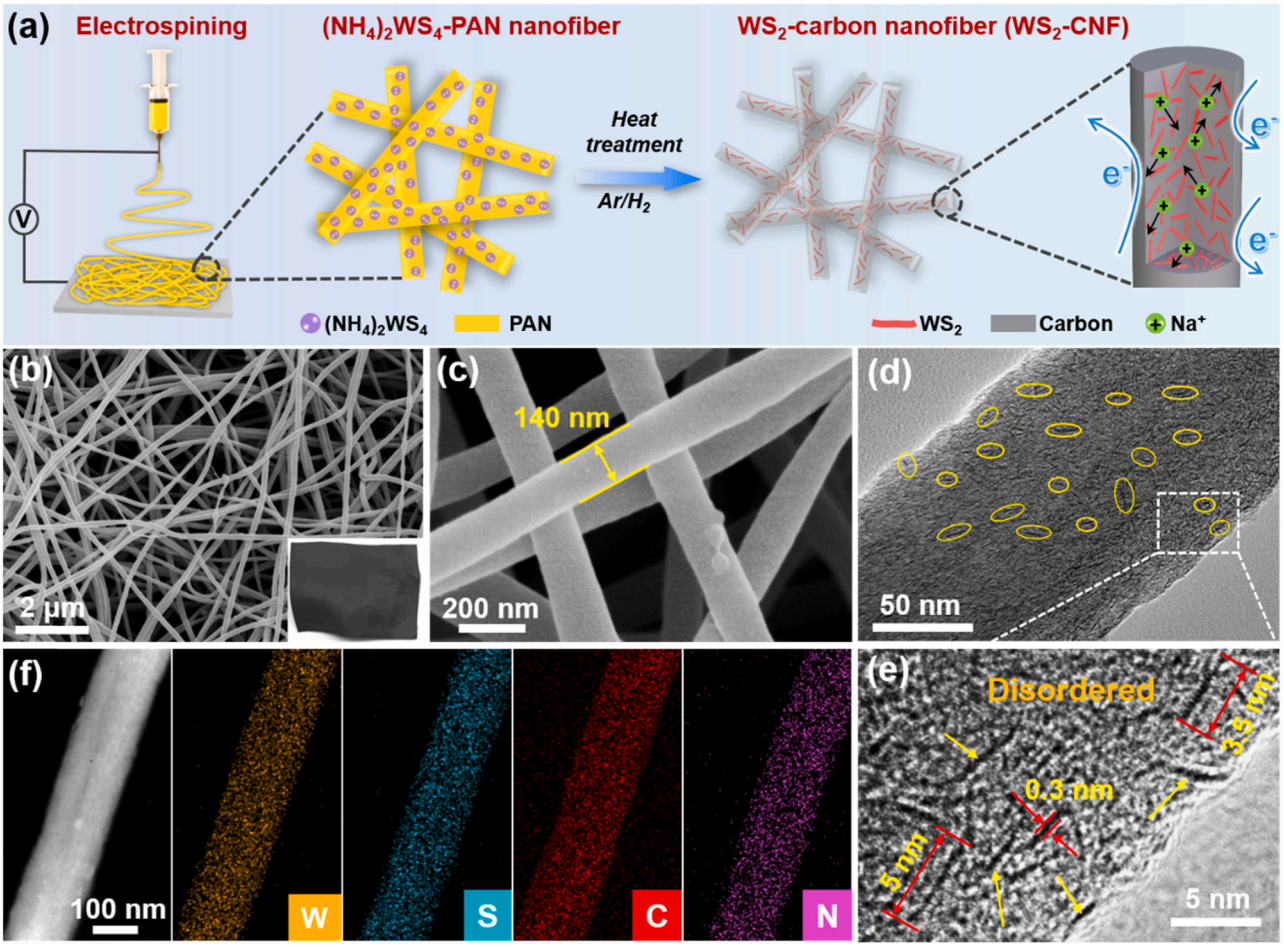

Fig. 1. Preparation and characterization of WS_2-CNF: (a) The synthesis process. (b, c) SEM images at different magnifications. The inset of (b) shows an optical photograph. (d, e) TEM images and (f) the corresponding EDS elemental mappings.

WS_2 nanosheets, which are marked by yellow circles, are uniformly dispersed in the CNF matrix (Fig. 1d, e). Moreover, the lateral dimension and thickness of these WS_2 nanosheets are measured as 3.5–5.0 nm and 0.3 nm, respectively. The thickness of 0.3 nm is identical to the distance between two S layers of WS_2, thereby indicating its monolayered structure [27,28]. The ultrafine and monolayered WS_2 nanosheets exhibit enriched edges and short mass transfer paths for favorable Na^+ storage [29,30]. In contrast, pure WS_2 shows a micron-sized bulk structure (Fig. S3a, b). The crystalline size and order degree of WS_2 obviously increase, with 4–10 layers and lateral dimensions of 10–30 nm (Fig. S3c, d). EDS elemental mappings further confirm the uniform dispersion of W, S, C, and N elements in the WS_2-CNF composite (Fig. 1f). In particular, the N element is derived from the pyrolysis of the PAN precursor, which contains N atoms. Furthermore, the pore structures of WS_2-CNF and WS_2-bulk are studied by BET analysis (Fig. S4). The WS_2-CNF composite shows a typical type IV isotherm with a surface area of 40.56 $m^2\ g^{-1}$ (Fig. S4a), which indicates a mesoporous structure. The corresponding pore size distribution of WS_2-CNF is measured by BJH method (Fig. S4b), which is narrow and indicates an average pore diameter of 3.83 nm. In contrast, the pure WS_2-bulk sample shows the characteristics of a nonporous powdery structure, and the surface area is only 3.18 $m^2\ g^{-1}$. The large surface area of WS_2-CNF can provide more active sites for Na^+ storage.

In Fig. 2a, the XRD pattern of WS_2-bulk shows three obvious diffraction peaks at $2\theta = 14.3°$, 33.6° and 58.5°, which are well indexed to the (002), (100) and (110) planes of hexagonal WS_2 (PDF# 08-0237), respectively [31,32]. Compared with WS_2-bulk, the weak characteristic peaks of WS_2-CNF are obviously broadened, indicating the formation of low-crystallinity WS_2. Meanwhile, the (002) plane peak disappears, further confirming its monolayered structure [27]. In addition, a small bump peak at $2\theta = 25°$ is observed for the WS_2-CNF composite, which is assigned to the typical (002) plane of carbon materials [33]. The crystal structure is further studied by Raman spectroscopy (Fig. 2b). The WS_2-bulk shows two strong peaks at 351 and 416 cm^{-1}, which arise from the typical in-plane (E^1_{2g}) and out-of-plane (A_{1g}) vibrational modes of WS_2 [31]. Nevertheless, the intensities of the E^1_{2g} and A_{1g} peaks for WS_2-CNF distinctly become weak, indicating that the strength of vibrating groups of WS_2 per unit area decreases with reduced crystallinity. In addition, WS_2-CNF exhibits two additional peaks at 1359 cm^{-1} (D-band) and 1595 cm^{-1} (G-band), which correspond to disordered and graphitic carbon, respectively [15]. These results further confirm the successful formation of the WS_2-CNF composite. WS_2 content in the WS_2-CNF composite is evaluated by TGA, as shown in Fig. 2c. By increasing the test temperature in air from 35 °C to 800 °C, a residual weight of 93.3 wt% is achieved for the pure WS_2-bulk sample, which is accompanied by the oxidization of WS_2 into WO_3 [34]. For the WS_2-CNF composite, the weight loss increases to 62.1 wt%, which originates from the oxidation of WS_2 and the decomposition of the CNF matrix. Thus, the WS_2 content is calculated to be 66.6 wt% in the WS_2-CNF composite. XPS spectra are conducted to probe the chemical composition and valence of WS_2-CNF. The distinct signals of W, S, C and N elements are detected in survey spectrum of WS_2-CNF (Fig. 2d). In the high-resolution W 4f and W 5p spectra of WS_2-CNF (Fig. 2e), two pairs of peaks at 33.0/35.2 eV and 36.1/38.0 eV

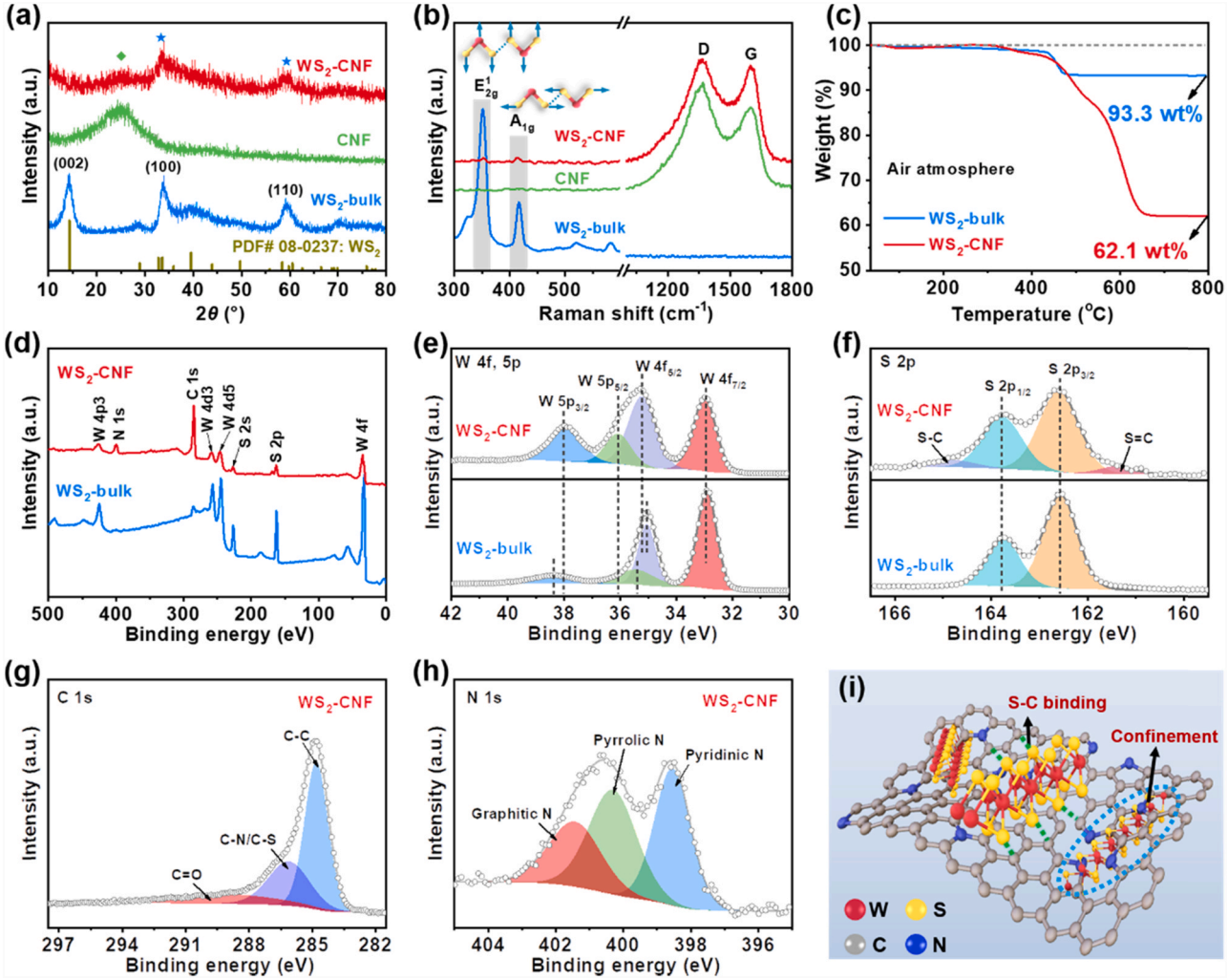

Fig. 2. (a) XRD patterns and (b) Raman spectra of WS_2-bulk, CNF and WS_2-CNF. (c) TGA of WS_2-bulk and WS_2-CNF. XPS spectra of WS_2-bulk and WS_2-CNF: (d) Survey spectrum, (e) W 4f and W 5p, (f) S 2p, (g) C 1s, and (h) N 1s (i) Schematic illustration of the WS_2-CNF structure.

correspond to W^{4+} [35]. Moreover, the W $4f_{5/2}$ and W 5p peaks for WS_2-CNF exhibit a slight shift compared with those of WS_2-bulk, which are associated with the electronic coupling between WS_2 and the carbon matrix [32]. In the S 2p spectra (Fig. 2f), the peaks at 162.6 and 163.8 eV are assigned to S^{2-}. Meanwhile, other shoulder peaks at 161.4 and 165.8 eV, which are derived from S═C and S–C, are observed in the WS_2-CNF composite, confirming the covalent bonding between the carbon matrix and WS_2 phase [31,36]. From the C 1s spectrum of WS_2-CNF (Fig. 2g), the peaks of C–C, C–N/C–S and C═O are detected at 284.8, 286.1 and 289.0 eV, respectively [37]. The existence of a C-N bond indicates N doping into the carbon lattice along with pyrolysis of the PAN precursor. Furthermore, the N 1s spectrum of WS_2-CNF (Fig. 2h) shows three typical peaks at 398.5, 400.3 and 401.4 eV, which are assigned to pyridinic N, pyrrolic N and graphitic N, respectively. It has been proven that N doping can introduce surface defects and improve the conductivity of materials, thereby effectively enhancing the Na^+ storage ability [38,39]. All the above analyses reasonably prove that the formation of low-crystallinity WS_2 nanosheets is confined to the CNF matrix through stable S-C bonding, as illustrated in Fig. 2i. With these structural features, the WS_2-CNF composite is expected to be used for high-performance SIB anodes.

3.2. Electrochemical sodium-ion storage performance of the WS_2-CNF composites

To investigate Na^+ storage performance of WS_2-CNF, CV measurements are firstly carried out (Fig. 3a). In the first cathodic scan, a strong cathodic peak at ~1.07 V is observed. This is related to the formation of a solid electrolyte interface (SEI) layer on the electrode surface and Na^+ insertion to form Na*x*WS_2 [40,41]. Subsequently, the cathodic peak at ~0.54 V is associated with the conversion reaction of Na*x*WS_2 into Na_2S and W [42]. The anodic peaks at 1.83 and 2.18 V are corresponding to the extraction of Na^+ and reversible reversion reactions to form WS_2. The sodium-ion storage mechanism of WS_2-CNF is further confirmed by *ex-situ* XRD analysis (Fig. S5), which is consistent with the reported literature [15,39]. Compared with the CV curves of WS_2-bulk (Fig. S6), WS_2-CNF exhibits obviously broadened redox peaks, implying a broad distribution of energy levels in the low-crystallinity WS_2 particles [43]. In the following cycles, the redox peaks of WS_2-CNF almost overlap, indicating excellent electrochemical reversibility. In contrast, WS_2-bulk shows an obvious variation and shift in profiles, demonstrating the inferior cycling stability on account of the structural degradation and polarization. Figs. 3b and S7 display the charge/discharge curves of the two

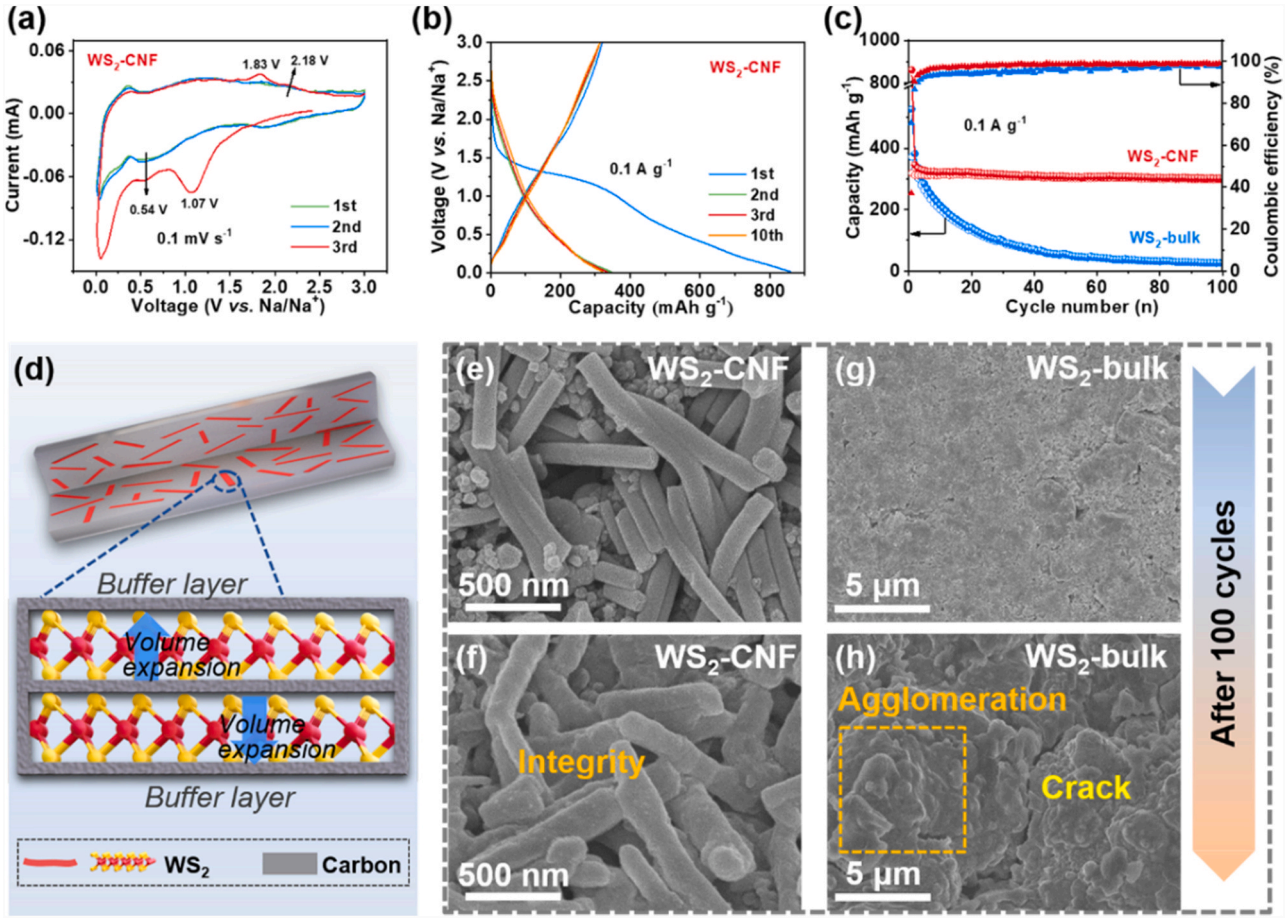

Fig. 3. (a) CV curves at 0.1 mV s^{-1} and (b) charge/discharge curves at 0.1 A g^{-1} of WS_2-CNF. (c) Cycling performance of the WS_2-bulk and WS_2-CNF electrodes at 0.1 A g^{-1}. (d) Schematic illustration of the enhanced structural stability of WS_2-CNF in SIBs. SEM images of (e, f) WS_2-CNF and (g, h) WS_2-bulk electrodes before cycling and after 100 cycles.

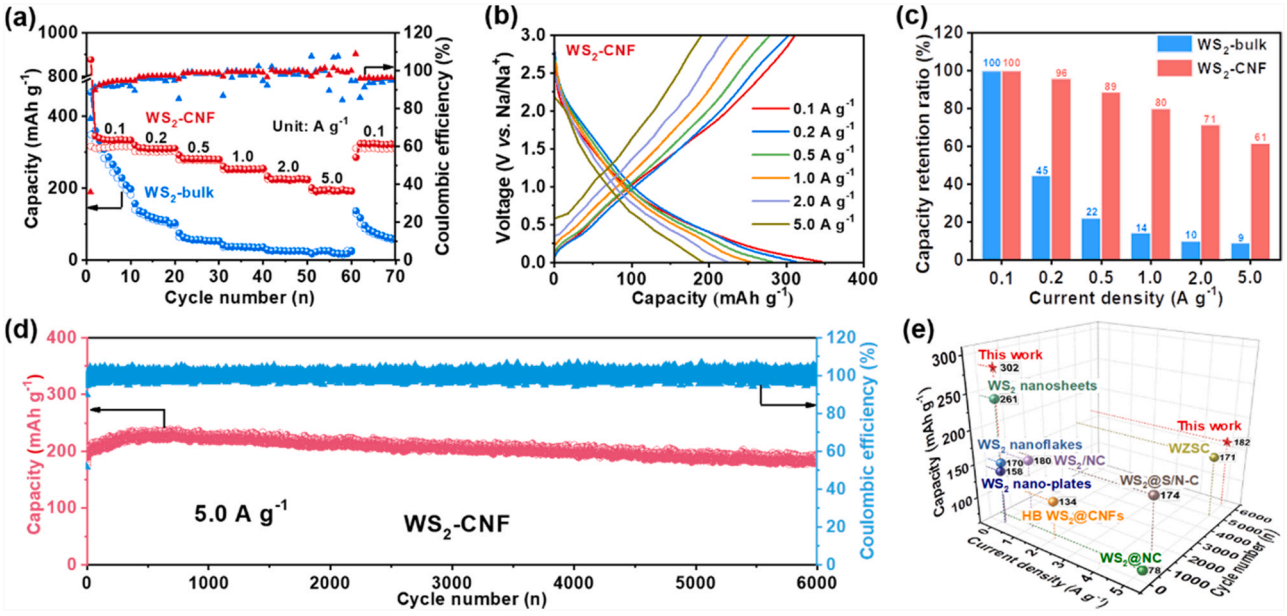

Fig. 4. (a) Rate performance, (b) charge/discharge curves and (c) capacity retention ratios at various densities (*vs.* 0.1 A g^{-1}) of the WS_2-CNF and WS_2-bulk electrodes. (d) Long cycling performance of WS_2-CNF at 5.0 A g^{-1}. (e) Cycling performance comparison between WS_2-CNF and the other reported WS_2-based anodes.

electrodes at 0.1 A g^{-1}. Initial discharge/charge capacities of 860/319 mAh g^{-1} and 527/372 mAh g^{-1} are obtained for WS_2-CNF and WS_2-bulk, with the initial Coulombic efficiency to be 37.1% (WS_2-CNF) and 70.6% (WS_2-bulk). For comparison, a galvanostatic charge/discharge test of the pure CNF electrode is carried out under the same conditions to obtain initial discharge/charge capacities of 460/197 mAh g^{-1} (Fig. S8a). Based on the WS_2 mass, the initial discharge/charge capacities of WS_2-CNF are calculated to be 1061/380 mAh g^{-1}.

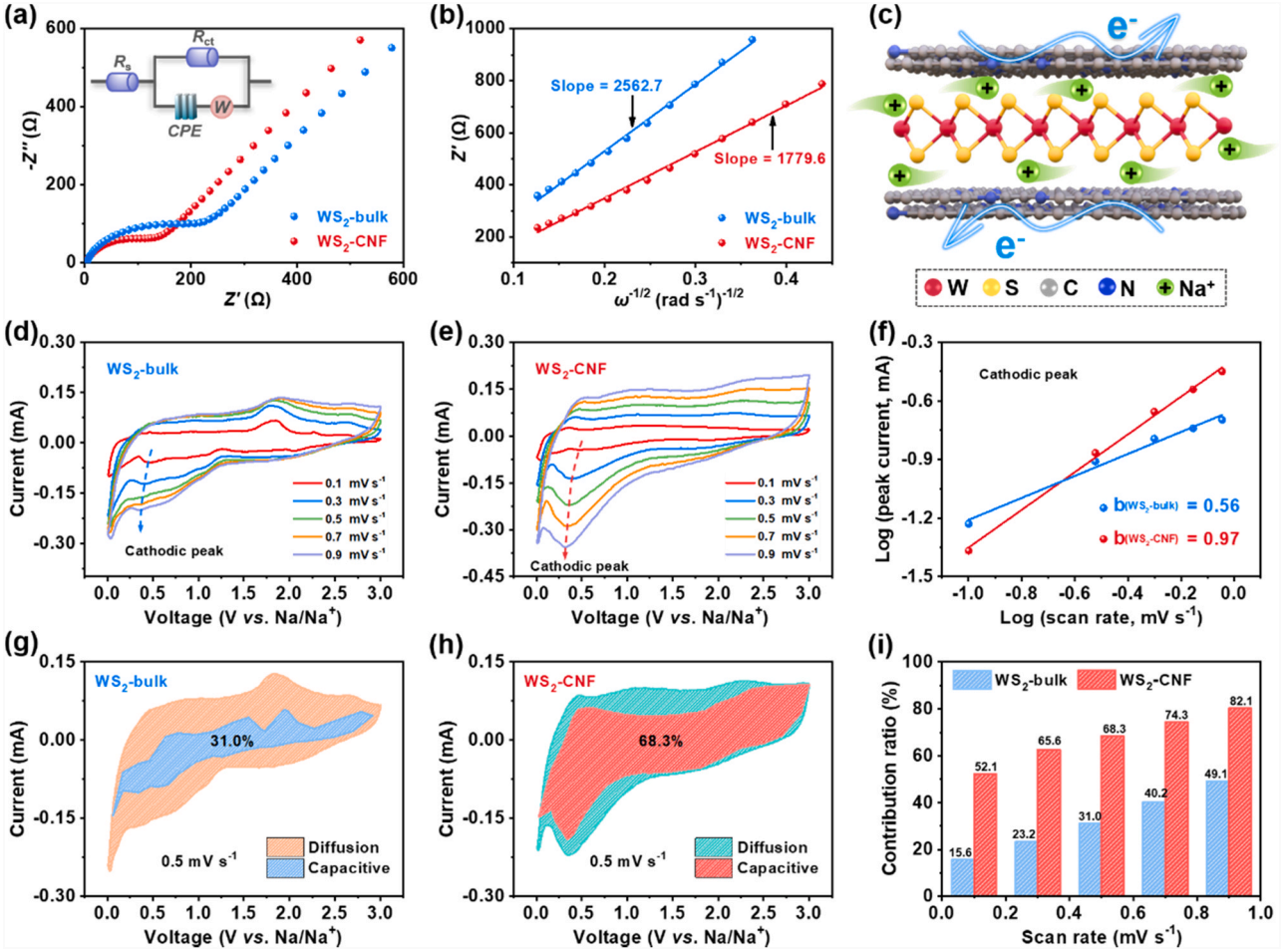

Fig. 5. Kinetic analysis of the WS_2-CNF electrode. (a) Nyquist plots and (b) Z' *vs.* $\omega^{-1/2}$ plots of the WS_2-bulk and WS_2-CNF electrodes. (c) Schematic illustration of Na^+/electron pathways in WS_2-CNF. CV curves at various scan rates for (d) the WS_2-bulk and (e) WS_2-CNF electrodes. (f) Log(*i*) *vs.* log(*v*) plots for the WS_2-bulk and WS_2-CNF electrodes. Capacitive contributions of (g) the WS_2-bulk and (h) WS_2-CNF electrodes at 0.5 mV s^{-1}. (i) Comparison of capacitive contribution ratios between the WS_2-bulk and WS_2-CNF electrodes at various scan rates.

Compared with the highly crystalline WS_2-bulk, the low-crystallinity WS_2 in the WS_2-CNF composite contributes to a higher capacity, which originates from its increased active sites for Na^+ storage. However, the low initial Coulombic efficiency value of WS_2-CNF is caused by the formation of a stable SEI layer [44], which leads to a large irreversible capacity loss. Encouragingly, the stable SEI layer can effectively protect the electrode from adverse side reactions with electrolyte, thus enhancing the electrochemical reversibility of the material [45]. Obviously, the WS_2-CNF electrode shows overlapped charge/discharge curves in the subsequent cycles and the Coulombic efficiency rapidly rises to 96.7% at the 10th cycle, confirming the high reversibility of its sodiation/desodiation process. After 100 cycles (Fig. 3c), WS_2-CNF maintains a discharge capacity of 302 mAh g^{-1} with a capacity retention of 94.7%, much superior to the WS_2-bulk electrode (26 mAh g^{-1} with a capacity retention of 6.9%). The capacity of CNF remains 186 mAh g^{-1} after 100 cycles with a retention of 94.4% (Fig. S8b). The cycling stability of WS_2-CNF is significantly improved, although the introduction of CNF slightly decreases the initial capacity. This is reasonably attributed to the confinement effect of the CNF matrix. As illustrated in Fig. 3d, low-crystallinity WS_2 reduces the volume expansion effect, while the buffer layer of the CNF matrix further reinforces its structural stability. The morphologies of the electrodes after cycling reveal that the integrity of WS_2-CNF is well maintained (Fig. 3e, f), while WS_2-bulk appears to agglomerate and crack (Fig. 3g, h).

The rate performances of WS_2-bulk and WS_2-CNF electrodes are compared in Fig. 4a. WS_2-CNF exhibits superior capacities of 315, 302, 279, 252, 225 and 194 mAh g^{-1} from 0.1 to 5.0 A g^{-1}. When the current reverts to 0.1 A g^{-1}, WS_2-CNF rapidly recovers to a stable value of 311 mAh g^{-1}, indicating its enhanced tolerance for fast sodiation/desodiation. In addition, the WS_2-CNF electrode exhibits similar voltage curves at various current densities (Figs. 4b and S9) and still maintains a large capacity retention of 61%, even at 5.0 A g^{-1} (Fig. 4c), further verifying its small electrochemical polarization. The WS_2-CNF electrode also retains a capacity of 182 mAh g^{-1} after 6000 cycles at 5.0 A g^{-1} (Fig. 4d). Moreover, the cycling performance of the WS_2-CNF anode with a higher loading is further tested (Fig. S10). When the mass loading increases to ~2.0 mg cm^{-2}, WS_2-CNF still performs efficiently and delivers a reversible capacity of 151 mAh g^{-1} after 3000 cycles at 5.0 A g^{-1} (Fig. S10a), with a high areal capacity of 0.3 mAh cm^{-2} (Fig. S10b). Therefore, the as-prepared WS_2-CNF anode can realize stable Na^+ storage process even at a high loading amount. Compared with other WS_2-based anodes in SIBs (Fig. 4e and Table S1), the WS_2-CNF anode shows outstanding high-rate and long-cycling performances.

3.3. *Exploring the kinetic behavior of WS_2-CNF*

To further explore the reason for the excellent rate performance of WS_2-CNF, EIS measurements are conducted. Fig. 5a displays

Nyquist plots of the electrodes and the equivalent circuit diagram. The fitting results show a smaller charge-transfer resistance (R_{ct}) for WS_2-CNF (138 Ω) than WS_2-bulk (217 Ω). Moreover, the diffusion coefficient (D_{Na^+}) is calculated based on Eq. (1–3) [46,47].

$$\omega=2\pi f \quad (1)$$

$$Z'=R+\sigma\omega^{-1/2} \quad (2)$$

$$D_{Na^+} = 0.5\ R^2T^2/S^2n^4F^4C^2\sigma^2 \quad (3)$$

S is the contact area between the electrode and electrolyte. n and C is the number of transferred electrons and molar concentration of Na^+, respectively. R, T and F are standard constants. The value of σ is determined by the slope of Z' *vs.* $\omega^{-1/2}$ (Fig. 5b). Thus, D_{Na^+} of WS_2-CNF is calculated to be 6.76×10^{-16} $cm^2\ s^{-1}$, being larger than that of WS_2-bulk (3.26×10^{-16} $cm^2\ s^{-1}$). These results confirm the improved kinetics in the WS_2-CNF electrode, which are ascribed to the rich active sites derived from the low-crystallinity WS_2 nanosheets and the favorable electron pathway provided by CNF (Fig. 5c). CV tests at various scan rates are performed to further study the electrochemical behavior of WS_2-bulk and WS_2-CNF electrodes (Fig. 5d, e). The measured response current (i) and scan rate (v) comply with Eq. (4), in which the b value can estimate the electrochemical behavior [48]. The b value is determined from the plot of log(i) *vs.* log(v). As displayed in Fig. 5f., the cathodic b-value of WS_2-CNF is 0.97, being close to 1, which indicates that the Na^+ storage process is dominated by surface pseudocapacitive behavior. For the WS_2-bulk electrode, the b value is 0.56, being near 0.5 and suggesting a diffusion-dominated Na^+ intercalation process. Based on Eqs. (5, 6) [40,48], the capacities from diffusion-/capacitive-controlled process can be quantitatively distinguished.

$$i = av^b \quad (4)$$

$$i = k_1v + k_2v^{1/2} \quad (5)$$

$$i/v^{1/2} = k_1v^{1/2} \quad (6)$$

As calculated, a capacitive contribution of 31.0% is obtained for WS_2-bulk at 0.5 mV s^{-1} (Fig. 5g), while that of WS_2-CNF is as high as 68.3% (Fig. 5h). Increasing the scan rates, the capacitive contributions of WS_2-CNF gradually rise and are always higher than those of WS_2-bulk. These results prove that rapid Na^+ uptake and release occur on the surface of WS_2-CNF, which further explains the reason of excellent rate performance.

4. Conclusions

In summary, the WS_2-CNF anode material for SIBs was facially synthesized *via* a universal electrospinning technique. Low-crystallinity and small-size WS_2 nanosheets were uniformly and stably confined in the conductive CNF matrix. The unique architecture of WS_2-CNF can alleviate the volume expansion effect during the cycling process, accelerate Na^+/electron transport and enhance the pseudocapacitive contribution. Consequently, the WS_2-CNF anode displays high-rate performance of 194 mAh g^{-1} at 5.0 A g^{-1} and an ultralong cycling life of 182 mAh g^{-1} after 6000 cycles. The remarkable performance makes WS_2-CNF anodes a great potential for advanced SIBs, while this work also provides an innovative path for the development of other electrode materials.

CRediT authorship contribution statement

Lulu Mo: Conceptualization, Validation, Formal analysis, Writing – original draft. **Mingyu Gao:** Validation, Investigation. **Gangyong Zhou:** Formal analysis, Investigation. **Wei Zong:** Formal analysis. **Ailong Chen:** Writing – review & editing. **Xiaoshan Fan:** Writing – review & editing, Supervision. **Yue-E. Miao:** Writing – review & editing, Supervision, Funding acquisition. **Tianxi Liu:** Writing – review & editing, Supervision.

Declaration of Competing Interest

The authors declare that they have no known competing financial interests or personal relationships that could have appeared to influence the work reported in this paper.

Acknowledgments

This work was financially supported by the National Natural Science Foundation of China (22075042), Natural Science Foundation of Shanghai (20ZR1401400), the Fundamental Research Funds for the Central Universities and DHU Distinguished Young Professor Program (LZB2021002).

Appendix A. Supporting information

Supplementary data associated with this article can be found in the online version at doi:10.1016/j.jallcom.2021.163518.

References

[1] Y. Tian, G. Zeng, A. Rutt, T. Shi, H. Kim, J. Wang, J. Koettgen, Y. Sun, B. Ouyang, T. Chen, Z. Lun, Z. Rong, K. Persson, G. Ceder, Promises and challenges of next-generation "beyond Li-ion" batteries for electric vehicles and grid decarbonization, Chem. Rev. 121 (2021) 1623–1669.
[2] R. Thangavel, M. Moorthy, B.K. Ganesan, W. Lee, W.S. Yoon, Y.S. Lee, Nanoengineered organic electrodes for highly durable and ultrafast cycling of organic sodium-ion batteries, Small 16 (2020) 2003688.
[3] H.S. Hirsh, Y. Li, D.H.S. Tan, M. Zhang, E. Zhao, Y.S. Meng, Sodium-ion batteries paving the way for grid energy storage, Adv. Energy Mater. 10 (2020) 2001274.
[4] J. Tian, H. Yang, C. Fu, M. Sun, L. Wang, T. Liu, In-situ synthesis of microspherical Sb@C composite anode with high tap density for lithium/sodium-ion batteries, Compos. Commun. 17 (2020) 177–181.
[5] P. Luo, C. Zheng, J. He, X. Tu, W. Sun, H. Pan, Y. Zhou, X. Rui, B. Zhang, K. Huang, Structural engineering in graphite-based metal-ion batteries, Adv. Funct. Mater. (2021) 2107277, https://doi.org/10.1002/adfm.202107277
[6] S. Kim, Y.J. Kim, W.H. Ryu, Controllable insertion mechanism of expanded graphite anodes employing conversion reaction pillars for sodium-ion batteries, ACS Appl. Mater. Interfaces 13 (2021) 24070–24080.
[7] R. Thangavel, A.G. Kannan, R. Ponraj, G. Yoon, V. Aravindan, D.W. Kim, K. Kang, W.S. Yoon, Y.S. Lee, Surface enriched graphene hollow spheres towards building ultra-high power sodium-ion capacitor with long durability, Energy Storage Mater. 25 (2020) 702–713.
[8] L. Bai, Y. Sun, L. Tang, X. Zhang, J. Guo, Sulfur and nitrogen co-doped carbon nanosheets for improved sodium ion storage, J. Alloy. Compd. 868 (2021) 159080.
[9] R. Thangavel, A.G. Kannan, R. Ponraj, M.S. Park, H. Choi, D.W. Kim, Y.S. Lee, High volumetric quasi-solid-state sodium-ion capacitor under high mass loading conditions, Adv. Mater. Interfaces 5 (2018) 1800472.
[10] M. Ma, Y. Yao, Y. Wu, Y. Yu, Progress and prospects of transition metal sulfides for sodium storage, Adv. Fiber Mater. 2 (2020) 314–337.
[11] W. Deng, J. Chen, L. Yang, X. Liang, S. Yin, X. Deng, G. Zou, H. Hou, X. Ji, Solid solution metal chalcogenides for sodium-ion batteries: the recent advances as anodes, Small 17 (2021) 2101058.
[12] R. Thangavel, A. Samuthira Pandian, H.V. Ramasamy, Y.S. Lee, Rapidly synthesized, few-layered pseudocapacitive SnS_2 anode for high-power sodium ion batteries, ACS Appl. Mater. Interfaces 9 (2017) 40187–40196.
[13] W. Zong, C. Yang, L. Mo, Y. Ouyang, H. Guo, L. Ge, Y. Miao, D. Rao, J. Zhang, F. Lai, T. Liu, Elucidating dual-defect mechanism in rhenium disulfide nanosheets with multi-dimensional ion transport channels for ultrafast sodium storage, Nano Energy 77 (2020) 105189.
[14] Z. Chen, X. Wang, H. Wang, H. Wang, T. Bai, F. Ren, P. Ren, H. Yan, K. Xiao, Z. Shen, Chinese knot-like bimetallic $NiCo_2S_4$ grew on 3D graphene foam as high-performance electrode for Na^+ storage, J. Alloy. Compd. 891 (2022) 161988.
[15] X. Hu, Y. Liu, J. Li, G. Wang, J. Chen, G. Zhong, H. Zhan, Z. Wen, Self-assembling of conductive interlayer-expanded WS_2 nanosheets into 3D hollow hierarchical microflower bud hybrids for fast and stable sodium storage, Adv. Funct. Mater. 30 (2019) 1907677.
[16] H. Tao, J. Li, J. Li, Z. Hou, X. Yang, L. Fan, Metallic phase $W_{0.9}Mo_{0.1}S_2$ for high-performance anode of sodium ion batteries through suppressing the dissolution of polysulfides, J. Energy Chem. 66 (2022) 356–365.
[17] X. Luo, L. Cao, J. Huang, J. Li, P. Guo, Y. Wang, Z. Xu, K. Kajiyoshi, Exposing WS_2 nanosheets edge by supports carbon structure: Guiding Na^+ intercalation along

(002) plane for enhanced reaction kinetics and stability, Chem. Eng. J. 411 (2021) 128554.
[18] X. Xu, X. Li, J. Zhang, K. Qiao, D. Han, S. Wei, W. Xing, Z. Yan, Surfactant assisted electrospinning of WS_2 nanofibers and its promising performance as anode material of sodium-ion batteries, Electrochim. Acta 302 (2019) 259–1269.
[19] H. Li, X. Wen, F. Shao, S. Xu, C. Zhou, Y. Zhang, H. Wei, N. Hu, Interlayer-expanded MoS_2 vertically anchored on graphene via C-O-S bonds for superior sodium-ion batteries, J. Alloy. Compd. 877 (2021) 160280.
[20] H. Wu, X. Chen, C. Qian, H. Yan, C. Yan, N. Xu, Y. Piao, G. Diao, M. Chen, Confinement growth of layered WS_2 in hollow beaded carbon nanofibers with synergistic anchoring effect to reinforce Li^+/Na^+ storage performance, Small 16 (2020) 2000695.
[21] Y.V. Lim, Y. Wang, D. Kong, L. Guo, J.I. Wong, L.K. Ang, H.Y. Yang, Cubic-shaped WS_2 nanopetals on a prussian blue derived nitrogen-doped carbon nanoporous framework for high performance sodium-ion batteries, J. Mater. Chem. A 5 (2017) 10406–10415.
[22] X. Zhang, H. Shi, L. Liu, C. Min, S. Liang, Z. Xu, Y. Xue, C. Hong, Z. Cai, Construction of MoS_2/Mxene heterostructure on stress-modulated kapok fiber for high-rate sodium-ion batteries, J. Colloid Interface Sci. 605 (2022) 472–482.
[23] H. Wu, N. Xu, Z. Jiang, A. Zheng, Q. Shi, R. Lv, L. Ni, G. Diao, M. Chen, Space and interface confinement effect of necklace-box structural FeS_2/WS_2 carbon nanofibers to enhance Na^+ storage performance and electrochemical kinetics, Chem. Eng. J. 427 (2022) 131002.
[24] P. Mao, Y. Wang, P. Xiao, W. Zhang, S. Rao, Z. Wang, Construction of N-doped C@ MoS_2 heteroshell with the yolk of Sn nanoparticles as high-performance anodes for sodium-ion batteries, J. Alloy. Compd. 892 (2022) 162157.
[25] W. Li, J. Huang, L. Feng, L. Cao, S. He, 3D self-assembled VS_4 microspheres with high pseudocapacitance as highly efficient anodes for Na-ion batteries, Nanoscale 10 (2018) 21671–21680.
[26] X. Zhang, J. Wang, X. Wang, Y. Li, Y. Zhao, Z. Bakenov, G. Li, 3D ordered macroporous amorphous Nb_2O_5 as anode material for high-performance sodium-ion batteries, Appl. Surf. Sci. 567 (2021) 150862.
[27] S. Yu, J.W. Jung, I.D. Kim, Single layers of WS_2 nanoplates embedded in nitrogen-doped carbon nanofibers as anode materials for lithium-ion batteries, Nanoscale 7 (2015) 11945–11950.
[28] W. Yang, H. Lu, Y. Cao, P. Jing, Single-/few-layered ultrasmall WS_2 nanoplates embedded in nitrogen-doped carbon nanofibers as a cathode for rechargeable aluminum batteries, J. Power Sources 441 (2019) 227173.
[29] S. Zhou, J. Chen, L. Gan, Q. Zhang, Z. Zheng, H. Li, T. Zhai, Scalable production of self-supported WS_2/CNFs by electrospinning as the anode for high-performance lithium-ion batteries, Sci. Bull. 61 (2016) 227–235.
[30] L. Chen, Y. Liu, Z.N. Deng, H. Jiang, C.Z. Li, Edge-enriched MoS_2@C/rGO film as self-standing anodes for high-capacity and long-life lithium-ion batteries, Sci. China Mater. 64 (2021) 96–104.
[31] X. Li, Y. Sun, X. Xu, Y.X. Wang, S.L. Chou, A. Cao, L. Chen, S.X. Dou, Lotus rhizome-like S/N–C with embedded WS_2 for superior sodium storage, J. Mater. Chem. A 7 (2019) 25932–25943.
[32] Y. Song, S. Bai, L. Zhu, M. Zhao, D. Han, S. Jiang, Y. Zhou, Tuning pseudocapacitance via C–S bonding in WS_2 nanorods anchored on N, S codoped graphene for high-power lithium batteries, ACS Appl. Mater. Interfaces 10 (2018) 13606–13613.
[33] S. Liu, K. Wan, C. Zhang, T. Liu, Polyaniline-decorated 3D carbon porous network with excellent electrolyte wettability and high energy density for supercapacitors, Compos. Commun. 24 (2021) 100610.
[34] C. Wu, X. Zeng, P. He, L. Chen, W. Wei, Flexible WS_2@CNFs membrane electrode with outstanding lithium storage performance derived from capacitive behavior, Adv. Mater. Interfaces 5 (2018) 1701080.
[35] X. Wang, J. Huang, J. Li, L. Cao, W. Hao, Z. Xu, Improved Na storage performance with the involvement of nitrogen-doped conductive carbon into WS_2 nanosheets, ACS Appl. Mater. Interfaces 8 (2016) 23899–23908.
[36] P. Ge, L. Zhang, W. Zhao, Y. Yang, W. Sun, X. Ji, Interfacial bonding of metal-sulfides with double carbon for improving reversibility of advanced alkali-ion batteries, Adv. Funct. Mater. 30 (2020) 1910599.
[37] W. Qin, L. Han, H. Bi, J. Jian, X. Wu, P. Gao, Hydrogen storage in a chemical bond stabilized Co_9S_8-graphene layered structure, Nanoscale 7 (2015) 20180–20187.
[38] J. Wang, N. Wu, L. Han, C. Liao, X. Mu, Y. Kan, Y. Hu, Polyacrylonitrile@metal organic frameworks composite-derived heteroatoms doped carbon@encapsulated cobalt sulfide as superb sodium ion batteries anode, J. Colloid Interface Sci. 581 (2021) 552–565.
[39] Y. Liu, H. Wei, C. Wang, F. Wang, H. Wang, W. Zhang, X. Wang, C. Yan, B.H. Kim, F. Ren, Nitrogen-doped carbon coated WS_2 nanosheets as anode for high-performance sodium-ion batteries, Front. Chem. 6 (2018) 236.
[40] P.C. Li, C.M. Chen, S.S. Ding, Z. Huang, H.C. He, M.Q. Cai, Y. Cai, M. Zhang, Controllable deposition of FeV_2S_4 in carbon fibers for sodium-ion storage with high capacity and long lifetime, Sci. China Mater. 64 (2021) 1355–1366.
[41] J. Wang, L. Yu, Z. Zhou, L. Zeng, M. Wei, Template-free synthesis of metallic WS_2 hollow microspheres as an anode for the sodium-ion battery, J. Colloid Interface Sci. 557 (2019) 722–728.
[42] S. Ghosh, Z. Qi, H. Wang, S.K. Martha, V.G. Pol, WS_2 anode in Na and K-ion battery: Effect of upper cut-off potential on electrochemical performance, Electrochim. Acta 383 (2021) 138339.
[43] P. Ge, H. Hou, S. Li, L. Yang, X. Ji, Tailoring rod-like $FeSe_2$ coated with nitrogen-doped carbon for high-performance sodium storage, Adv. Funct. Mater. 28 (2018) 1801765.
[44] C. Zhu, P. Kopold, W. Li, P.A. van Aken, J. Maier, Y. Yu, Engineering nanostructured electrode materials for high performance sodium ion batteries: a case study of a 3D porous interconnected WS_2/C nanocomposite, J. Mater. Chem. A 3 (2015) 20487–20493.
[45] W. Zhao, L. Zhang, F. Jiang, X. Chang, Y. Yang, P. Ge, W. Sun, X. Ji, Engineering metal sulfides with hierarchical interfaces for advanced sodium-ion storage systems, J. Mater. Chem. A 8 (2020) 5284–5297.
[46] G. Zhou, L. Mo, C. Zhou, Y. Lv, Y. Miao, T. Liu, Flexible naphthalene-based polyimide nanofiber cathode with hierarchical micro/nanoporous structure for high-performance organic sodium-ion batteries, Compos. Commun. 22 (2020) 100490.
[47] Q. Pan, M. Zhang, L. Zhang, Y. Li, Y. Li, C. Tan, F. Zheng, Y. Huang, H. Wang, Q. Li, $FeSe_2$@C microrods as a superior long-life and high-rate anode for sodium ion batteries, ACS Nano 14 (2020) 17683–17692.
[48] W. Zong, N. Chui, Z. Tian, Y. Li, C. Yang, D. Rao, W. Wang, J. Huang, J. Wang, F. Lai, T. Liu, Ultrafine MoP nanoparticle splotched nitrogen-doped carbon nanosheets enabling high-performance 3D-printed potassium-ion hybrid capacitors, Adv. Sci. 8 (2021) 2004142.